



ELSEVIER

Contents lists available at ScienceDirect

Powder Technology

journal homepage: [www.elsevier.com/locate/powtec](http://www.elsevier.com/locate/powtec)

# Characterization of a sediment layer of concentrated fluid-solid mixtures in tilted ducts at low Reynolds numbers



Sergio Palma<sup>a,b,\*</sup>, Christian F. Ihle<sup>c,a</sup>, Aldo Tamburrino<sup>d,a</sup>

<sup>a</sup> Advanced Mining Technology Center, University of Chile, Santiago, Chile

<sup>b</sup> School of Civil Engineering, The University of Queensland, Brisbane, Australia

<sup>c</sup> Department of Mining Engineering, University of Chile, Santiago, Chile

<sup>d</sup> Department of Civil Engineering, University of Chile, Santiago, Chile

## ARTICLE INFO

### Article history:

Received 15 February 2017

Received in revised form 23 October 2017

Accepted 29 October 2017

Available online 1 December 2017

### Keywords:

Fluid dynamics

Sedimentation

Boycott effect

Duct obstruction

Solid-fluid mixtures model

## ABSTRACT

In this paper we use a continuum mixture model to solve numerically the momentum and continuity equations associated with the sedimentation dynamics of highly concentrated fluid-solid mixtures in tilted ducts at low Reynolds numbers. The set of numerical simulations include several combinations of fluid viscosity, duct angle and solid concentration of particles. This research aims to show the phenomenology and dynamics associated with the sedimentation of monodisperse particles under different physical conditions and the characterization of the final stage of the sediment layer in two kinds of inclined geometries, with and without a horizontal section. Using scaling arguments, a mathematical expression formed by three dimensionless groups including the inertial number, particle concentration and the ratio between the sedimentation Grashof number to the Reynolds number is proposed to explain the height of the sediment layer in the slope change zone of a duct. Additionally, we have found that the initial particle concentration is a very relevant variable for knowing under what conditions the duct could get obstructed. In combination with some system angles, they might represent a risk of duct plug. Imposing a condition of obstruction, we have found dimensionless parameters that result in the blockage of the duct in the slope change zone. The results can be applied in the transport of fluid-solid mixtures and, in the engineering design of ducts with abrupt slope changes.

© 2017 Elsevier B.V. All rights reserved.

## 1. Introduction

The hydraulic transport of solids at high concentrations (e.g., ore concentrates and tailings) is a widely used technique in the mining and dredging industry. Normally, such method is carried out mixing the particles with water in order to enable the motion of the solid phase through pipelines and ducts [1]. This technology has been proven to be a cost-effective option for long distances and high throughput requirements. In the particular case of ore concentrates, pipelines can be as large as hundreds of kilometres long, and are commonly installed in natural topographies, which include the presence of low and high points. The design of this kind of infrastructure faces challenges including the need to keep solids in motion at all times [2] and to enable safe system startups after planned shutdowns or power outages. When the latter operational scenario occurs, it

is required during startup to remove the solids settled at high concentrations at the various low points in the system. The frictional resistance to motion in those points, where solids have settled and compacted, is higher than that corresponding to steady operation [3], and requires to be accounted for when selecting both pipeline and pumping equipment. Failure to cope with proper designs in long distance pipelines may cause ruptures due to blockages, thus affecting urban centers or natural resources such as lakes, rivers, and agriculture, potentially causing severe environmental problems and enormous damage to local communities [1,2,4]. Central to this point is the need to properly address the implications of high and low points through the development of engineering models for solids migration

Sedimentation is the process by which solid particles immersed in a fluid are deposited at the bottom by the action of gravity. Sedimentation is one of the oldest known techniques used in industry to clean fluids or, alternatively, to recover particles from suspensions [5]. In 1920, Boycott noted that certain blood corpuscles settled faster at the bottom in inclined test tubes than in test tubes that were in an upright position. This improvement in the sedimentation velocity is

\* Corresponding author at: Advanced Mining Technology Center, University of Chile, Santiago, Chile.

E-mail address: [sergio.palma@ing.uchile.cl](mailto:sergio.palma@ing.uchile.cl) (S. Palma).

due to that in an inclined duct, the suspension has a short distance to reach the lower side of the duct, before they start to slide down to the bottom of the duct, whereas in a upright duct all the sediment is slow and there is no vertically rapid sliding [6,7].

For almost five decades the behaviour of inclined settlers was described using a kinematic model called PNK in recognition of Ponder [8] and Nakamura & Kuroda [9] who developed it. A typical phenomenon observed in inclined settlers for laminar flow is displayed in Fig. 1. The PNK model states that the production rate of clear fluid per unit depth of a rectangular settler is given by  $S = w_0 F[\cos\theta + H \tan\theta/b]$ , where  $w_0$  is the sedimentation velocity of a particle,  $F$  is a hindered function which accounts for the interaction of many particles immersed in a fluid,  $\theta$  is the angle of inclination of the system,  $H$  is the instantaneous height of the suspension and  $b$  is the space between the walls of the duct. PNK theory often overestimates the efficiency of an inclined settler, however it does not consider the dynamics of fluid movement as it is based solely on a mass balance [10]. When a settler is inclined, a thin layer of clear fluid is formed along the upper wall. Due to the density of the fluid being less than the density of the suspension in the vicinity, a force is experienced which causes the fluid to accelerate upwards [11].

Resistance to this upward movement is given by the viscous and inertial forces acting within the clear fluid layer as well as the upper wall of the settler and regions of particle suspension. If the velocities within the layer of clear fluid are very large, it might be possible that waves appear along the interface between the suspension region and the clear fluid layer. These waves can grow and break as they ascend to the settler, thus dragging the suspension to the clear fluid layer and decreasing the efficiency of the settler [12]. In order to predict the performance of an inclined settler, it is necessary to describe the formation and growth of these instabilities.

Works related to the dynamics of suspensions in tilted settlers in the decade preceding ninety, can be found in Davis & Acrivos [13]. Current analytical theories to describe the dynamics of suspensions in tilted ducts are generally based on the analysis presented by Acrivos & Herzolzheimer [10], who studied the process using a simplified model. The equations used consist of a continuity equation for each phase, i.e., one for the solid phase and one for the fluid phase, an equation of momentum mixture describing the suspension of particles as a whole and a relationship between the velocities of each phase. Neglecting inertial effects and assuming that the suspension region has a uniform concentration of solids, these authors used boundary layer analysis to find expressions for the geometry and flow within the clear fluid layer. In addition, they determined

that the kinematics of the sedimentation process is described by two dimensionless groups, a sedimentation Reynolds number and quotient of a settler Grashof and Reynolds number, which are given by  $Re = Hw_0F\rho_f/\eta_f$  and  $\Lambda = H^2g(\rho_s - \rho_f)\phi/\eta_fw_0F$ , respectively. In this expression,  $\phi$  is the volume fraction of particles in the suspension zone. The hypothesis of negligible inertial forces established in the work of these authors implies that the analysis is limited to the settlers where  $\Lambda \gg 1$  and  $Re\Lambda^{-1/3} \ll 1$ .

Finally, they found that the rate of production of clear fluid would be predicted by the theory PNK whenever the interface between the suspension region and the clear fluid layer remains stable and  $\Lambda \rightarrow \infty$ . Herzolzheimer [12] developed this analysis to settlers under viscous conditions ( $Re\Lambda^{-1/3}$ ) and he compared his theoretical results with experimental results of instability waves on the interface. Later, Shaqfeh & Acrivos [14] included inertial effects and extended the theory for all values of  $Re\Lambda^{-1/3}$ . Comparisons between experimental and analytical results for the clear fluid layer predicted by this theory have been very satisfactory, particularly for the more viscous cases where  $Re\Lambda^{-1/3}$  is small. In this paper we have used a continuum mixture model to solve numerically the momentum and continuity equations associated with the sedimentation dynamics of high concentrated fluid-solid mixtures in tilted ducts. While previous works were able to describe the operation of settlers when the interface of clear fluid layer is stable, they do not define under what kind of conditions this occurs. Acrivos and other researchers have applied linear stability theory to the region surrounding the clear fluid layer to find conditions under which small perturbations in the interface will grow over time. Subsequently, Nir & Acrivos [15] did experiments on inclined surfaces and found that for given values of the concentration of particles in the suspension, the sediment flow remained constant only if the angle of the system exceeded a minimum value. Additionally, a discontinuity in the concentration of particles in the suspension was found. Afterwards, Kapoor & Acrivos [16] implemented the model proposed by Nir & Acrivos [15] but including the effects of shear-induced diffusion due to gradients in the shear stress likewise the slip velocity along the walls of the duct. The focus of this research is on the nonlinear dynamics associated with the migration of particles at low slopes, and in particular the consequences for axial transport of solid material under these conditions, with emphasis on the conditions for the generation of obstructions at high particle fractions. In Section 2, we provide the mathematical model used for our numerical simulations, and the numerical procedure used in our calculations. In Section 3, the results of our numerical simulations are presented and discussed. Finally, the conclusions are showed in Section 4.

**2. Governing equations**

A set of numerical simulations has been made using COMSOL Multiphysics with the CFD package for modelling the sedimentation of particles in tilted ducts [17,18]. The dynamics of a suspension can be modelled by two equations of momentum transfer, one for particles and the other for the fluid, plus a continuity equation for both phases. Assuming that the mass transfer between the two phases is zero, the continuity equations for the continuous and dispersed phase are, respectively,  $\partial_t(\rho_f\phi_f) + \nabla \cdot (\rho_f\phi_f\mathbf{u}_f) = 0$  and  $\partial_t(\rho_s\phi_s) + \nabla \cdot (\rho_s\phi_s\mathbf{u}_s) = 0$ , where  $\phi$  is the volume concentration,  $\rho$  is the density and  $\mathbf{u}$  is the velocity. The subscripts  $f$  and  $s$  refer to quantities associated with the continuous phase (fluid) and the dispersed phase (particles). In this model, both the continuous and the dispersed phase are considered incompressible. Therefore, the above equations can be simplified as,

$$\frac{\partial \phi_f}{\partial t} + \nabla \cdot (\phi_f \mathbf{u}_f) = 0, \tag{1}$$

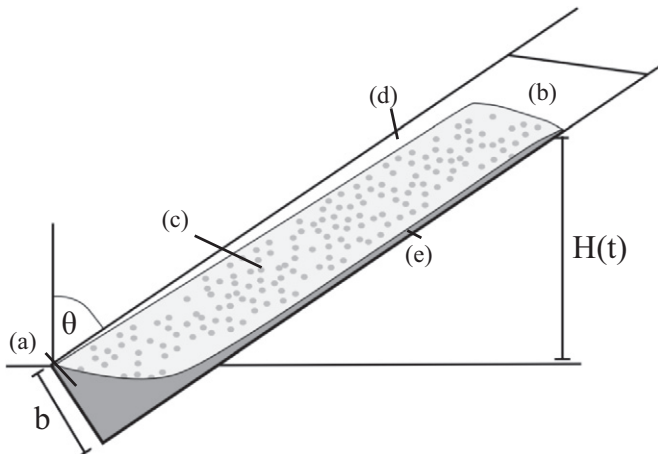


Fig. 1. Schematic of the conceptual model: (a) Sediment bed, (b) Clear fluid region, (c) Suspension region, (d) Clear fluid region and (e) Sediment layer.

$$\frac{\partial \phi_s}{\partial t} + \nabla \cdot (\phi_s \mathbf{u}_s) = 0. \quad (2)$$

If Eqs. (1) and (2) are coupled by the volume conservation condition  $\phi_f + \phi_s = 1$ , an equation of continuity for the mixture is obtained,

$$\nabla \cdot (\phi_s \mathbf{u}_s + \mathbf{u}_f(1 - \phi_s)) = 0. \quad (3)$$

The momentum equations for the continuous and dispersed phase, respectively, using the non-conservative form [17–22] are,

$$\rho_f \phi_f \left[ \frac{\partial \mathbf{u}_f}{\partial t} + (\mathbf{u}_f \cdot \nabla) \mathbf{u}_f \right] = -\phi_f \nabla p + \nabla \cdot (\phi_f \boldsymbol{\tau}_f) + \phi_f \rho_f \mathbf{g} + \mathbf{F}_{m,f}. \quad (4)$$

$$\rho_s \phi_s \left[ \frac{\partial \mathbf{u}_s}{\partial t} + (\mathbf{u}_s \cdot \nabla) \mathbf{u}_s \right] = -\phi_s \nabla p + \nabla \cdot (\phi_s \boldsymbol{\tau}_s) + \phi_s \rho_s \mathbf{g} + \mathbf{F}_{m,s}. \quad (5)$$

Here,  $p$  is the pressure of the mixture, which is assumed equal for both phases to simplify the calculations. The viscous stress tensor of each phase is indicated by  $\boldsymbol{\tau}$  in the momentum equations,  $\mathbf{g}$  is the acceleration due to gravity, and  $\mathbf{F}_m$  corresponds to the exchange of momentum between the phases, thus corresponding to a volume force exerted by one of the phases on the other phase. In the equations presented above, the influence of the polydispersity of the particles in the dispersed phase has been neglected. Eq. (5) can be written as [17,18],

$$\rho_s \phi_s \left[ \frac{\partial \mathbf{u}_s}{\partial t} + (\mathbf{u}_s \cdot \nabla) \mathbf{u}_s \right] = -\phi_s \nabla p + \nabla \cdot \boldsymbol{\tau}_s - \nabla p_s + \phi_s \rho_s \mathbf{g} + \mathbf{F}_{m,s}, \quad (6)$$

where  $p_s$  is the solid pressure, which will be explained in detail below. In the momentum equations described above, the continuous phase is considered Newtonian. This assumption is based in sedimentation experiments on viscous Newtonian fluids [23]. Hence, viscous stress tensor is defined as

$$\boldsymbol{\tau}_f = \eta_f \left[ \nabla \mathbf{u}_f + (\nabla \mathbf{u}_f)^T - \frac{2}{3} (\nabla \cdot \mathbf{u}_f) \mathbb{I} \right], \quad (7)$$

$$\boldsymbol{\tau}_s = \eta_s \left[ \nabla \mathbf{u}_s + (\nabla \mathbf{u}_s)^T - \frac{2}{3} (\nabla \cdot \mathbf{u}_s) \mathbb{I} \right], \quad (8)$$

where  $\eta$  is the dynamic viscosity of the respective phase and  $\mathbb{I}$  is the identity tensor [17,18]. In order to model the Newtonian viscosity associated to a set of particles in a mixture there is a variety of formulations. In this paper, we have worked with the model proposed by Krieger [24] because it is one of the most validated experimentally at high concentrations of particles over the years [25–27]. Specifically, we take

$$\eta_s = \eta_f \left( 1 - \frac{\phi_s}{\phi_{s,\max}} \right)^{-2.5\phi_{s,\max}}. \quad (9)$$

In order to avoid singularities in the numerical solutions when volume concentrations tend to zero, the momentum equations are divided by their corresponding volume concentrations. Therefore, Eq. (4), corresponding to the continuous phase, becomes

$$\rho_f \frac{\partial \mathbf{u}_f}{\partial t} + \rho_f (\mathbf{u}_f \cdot \nabla) \mathbf{u}_f = -\nabla p + \nabla \cdot \boldsymbol{\tau}_f + \frac{\nabla \phi_f \cdot \boldsymbol{\tau}_f}{\phi_f} + \rho_f \mathbf{g} + \frac{\mathbf{F}_{m,f}}{\phi_f}, \quad (10)$$

and Eq. (6), corresponding to the dispersed phase, becomes

$$\rho_s \frac{\partial \mathbf{u}_s}{\partial t} + \rho_s (\mathbf{u}_s \cdot \nabla) \mathbf{u}_s = -\nabla p + \nabla \cdot \left( \frac{\boldsymbol{\tau}_s}{\phi_s} \right) + \nabla \phi_s \cdot \left( \frac{\boldsymbol{\tau}_s}{\phi_s^2} \right) - \frac{\nabla p_s}{\phi_s} + \rho_s \mathbf{g} + \frac{\mathbf{F}_{m,s}}{\phi_s}. \quad (11)$$

The equations to be solved numerically simultaneously are Eqs. (3), (10) and (11). On the other hand, the term associated to the interphase momentum transfer, especially in fluids having a high concentration of particles, is given by the drag force, defined as  $\mathbf{F}_{m,f} = -\mathbf{F}_{m,s} = \beta(\mathbf{u}_s - \mathbf{u}_f)$ , where  $\beta$  is the drag coefficient. For fluids with a high concentration of particles by volume, it can be calculated by the method proposed by Gidaspow [28] in conjunction with the model proposed by Wen & Yu [29] for the drag coefficient

$$\beta = \begin{cases} \frac{150\eta_f\phi_s^2}{\phi_f d_s^2} + \frac{1.75\phi_s\rho_f|\mathbf{u}_{slip}|}{d_s} & \phi_s < 0.20, \\ \frac{3\phi_f\phi_s\rho_f c_D |\mathbf{u}_{slip}| \phi_f^{-2.65}}{4d_s} & \phi_s > 0.20. \end{cases} \quad (12)$$

Here,  $\mathbf{u}_{slip} = \mathbf{u}_s - \mathbf{u}_f$  is the relative velocity between the solid and liquid phases,  $d_s$  is the diameter of the particles and  $c_D$  is the drag coefficient for a single particle in an infinite medium. The drag coefficient is a function of the particle Reynolds number, which is determined from

$$c_D = \begin{cases} \frac{24}{Re_p} \left[ 1 + 0.15Re_p^{0.687} \right] & Re_p < 1000, \\ 0.44 & Re_p > 1000. \end{cases} \quad (13)$$

Furthermore, the local particle Reynolds number is defined as,  $Re_p = \phi_f d_s \rho_f |\mathbf{u}_{slip}| / \eta_f$ . For mixtures of particles and fluids, it is necessary to have a term associated with the interaction of particles. This term is commonly called solid pressure,  $p_s$ , [17,28]. The solid pressure term models the particle interaction due to collisions and friction, between the solid particles. The solid pressure model implemented herein uses a gradient diffusion based assumption in the manner of  $\nabla p_s = -\chi(\phi_f) \nabla \phi_f$ , whereas the empirical function  $\chi(\phi_f)$  has the form  $\chi(\phi_f) = 10^{a_1 \phi_f + a_2}$ . The function  $\chi(\phi_f)$  represents the modulus of elasticity for the dispersed phase [17,18,30]. Empirical values for the constants of this function have been obtained by different researchers [17,18,28,30,31]. Although there are several coefficients  $a_1$  and  $a_2$  in the literature, the numerical results of the sedimentation process do not change significantly depending on the choice [23]. Here,  $a_1 = -10.50$  and  $a_2 = 9.00$ , with  $\chi$  in Pa [32,33]. This model is valid in the international system of measures. Although this model is simple in its formulation, it has been able to model properly the behaviour of particles in a sedimentation process in inclined containers, (see Fig. 8, [23]).

The continuity equation of the mixture (3) and the momentum transport equations of both phases, Eqs. (10) and (11), are discretized by the Galerkin finite element method (FEM) [34]. The various simulation conditions have been given in Table 1. The boundary conditions associated with the computational domain can be seen in

**Table 1**  
Set of parameters of numerical simulations.

| Fluid-solid properties                          | Value                        |
|---|------------------------------|
| Particle density, $\rho_s$ (kg/m <sup>3</sup> ) | 1200                         |
| Fluid density, $\rho_f$ (kg/m <sup>3</sup> )    | 1000                         |
| Particle diameter, $d_s$ ( $\mu$ m)             | 600                          |
| Max. vol. fraction, $\phi_{s,\max}$             | 0.62                         |
| Angle system, $\theta_s$ (°)                    | [5, 10, 15, 20, 25, 30]      |
| Initial vol. fraction, $\phi_{s0}$ (%)          | [10, 15, 20, 25, 30, 35, 40] |
| Fluid viscosity, $\eta_f$ (mPa·s)               | [100, 200, 300]              |
| Numerical parameters                            | Value                        |
| Length scale 1, $L_0$ (mm)                      | 40                           |
| Length scale 2, $L_1$ (mm)                      | 500                          |
| Time step, $\Delta t$ (s)                       | 0.1                          |
| Simulation time, $T$ (s)                        | 800                          |

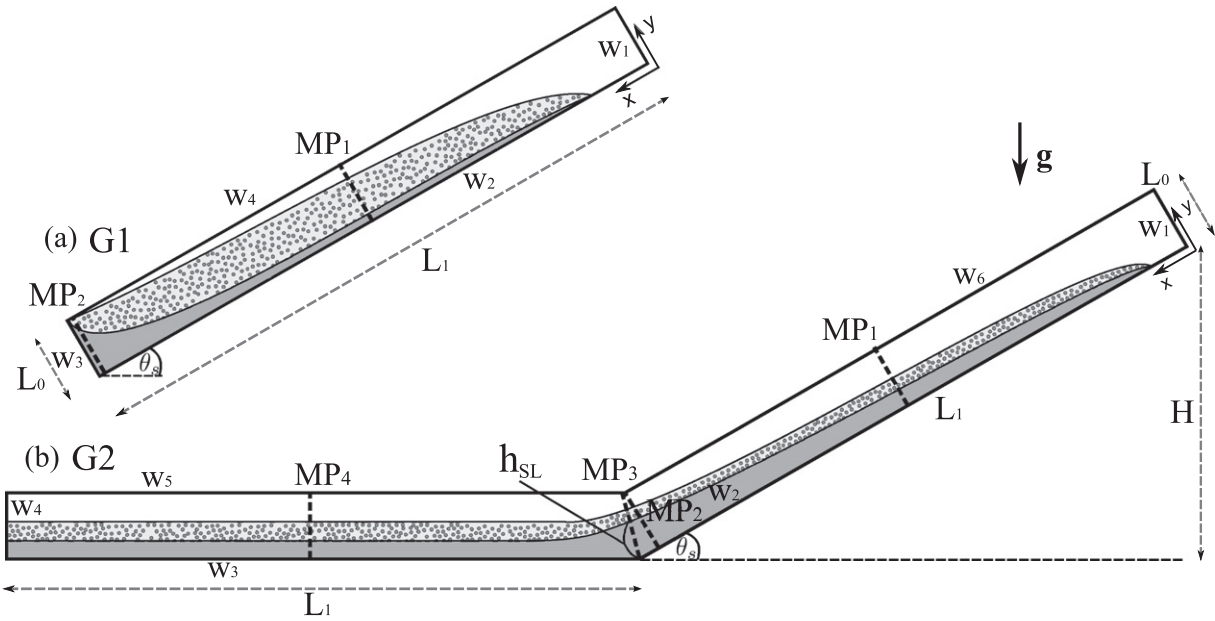


**Fig. 2.** Schematic of the conceptual model: (a) G1: Inclined duct geometry. (b) G2: Inclined duct geometry plus a horizontal section. The walls of the ducts and measurement profiles are represented by  $w_j$ , with  $j \in \{1, \dots, 6\}$  and  $MP_j$ , with  $j \in \{1, \dots, 4\}$ , respectively. The variable  $h_{SL}$  is used to test the convergence, as detailed in Fig. 3.

detail in Fig. 2. Firstly, we consider no-slip conditions and no penetration for both phases in all domain borders, so that  $\mathbf{u}_f = \mathbf{u}_s = 0$  at  $w_j$ , with  $j \in \{1, \dots, 6\}$ , where  $w_j$  stands for the surface defining the wall  $j$ . Regarding the dispersed phase, we imposed a condition of no-flow to outside the settler, i.e.,  $\phi_s \mathbf{u}_s \cdot \mathbf{n} = 0$  at  $w_j$  and  $(1 - \phi_s) \mathbf{u}_f \cdot \mathbf{n} = 0$  for the continuous phase. The system of equations has been integrated from 0 to 800 s, with a time step of 0.1 s which is about 1/4 of the time it takes a particle of the above features, to travel a distance equal to its own size at a velocity equal to the Stokes. However, due to the high storage space required for each of the simulations, only the information every 2 s has been stored. Eqs. (3), (10) and (11) are nonlinear convection-diffusion equations. These may become numerically unstable when the Galerkin method is used for discretization. Therefore, it is necessary to apply stabilization techniques to the finite element method in order to obtain physically meaningful solutions. There are three types of methods in COMSOL Multiphysics to numerically stabilize the equations of the form  $\partial_t u + (\beta \cdot \nabla) u = \nabla \cdot (c \nabla u) + F$ , namely isotropic diffusion, diffusion of streamlines and crosswind diffusion. In the above equation,  $\beta$  is the convective velocity vector,  $c$  is the diffusion coefficient and  $u$  is the scalar property transported. When the convection-diffusion equation is discretized using the Galerkin finite element method, numerical problems occur for Peclet numbers greater than 1 that necessarily should be controlled in each time step, [35].

The isotropic diffusion is equivalent to add a term,  $c_{art} = \delta_{id} h |\beta|$ , where  $h$  is the mesh size. Here,  $\delta_{id}$  is an adjustable parameter. Thus, the equation which is solved in simple terms is  $\partial_t u + (\beta \cdot \nabla) u = \nabla \cdot ((c + c_{art}) \nabla u) + F$ . It has used a value of  $\delta_{id} = 0.25$  in all simulations because it is the best parameter value that allows to obtain

properly the convergence of all calculations after a series of 30 preliminary tests. In order to choose an appropriate mesh size for the calculations, a set of simulations for different mesh sizes has been performed under four physical and numerical conditions as can be seen in Table 2. Fig. 3 shows the height of the sediment layer at location  $MP_3$  for the inclined geometry G2 (Fig. 2) as function of the number of mesh elements. The solid line in Fig. 3 represents the trend points for different physical conditions and the grey region represents the area of convergence of the numerical solutions.

Considering the input conditions of Table 2, it is observed that the height of the sediment layer reaches to  $h_{SL} \approx 35$  mm,  $h_{SL} \approx 33$  mm,  $h_{SL} \approx 30$  mm and  $h_{SL} \approx 10$  mm for Case 1, Case 2, Case 3 and Case 4, respectively, with about 10,000 mesh elements, whereas it rapidly

**Table 2**  
Set of conditions for convergence analysis.

|         | Angle                 | Initial volume fraction |
|---------|-----------------------|-------------------------|
| Case 1: | $\theta_s = 30^\circ$ | $\phi_0 = 0.40$         |
| Case 2: | $\theta_s = 5^\circ$  | $\phi_0 = 0.40$         |
| Case 3: | $\theta_s = 5^\circ$  | $\phi_0 = 0.30$         |
| Case 4: | $\theta_s = 10^\circ$ | $\phi_0 = 0.10$         |

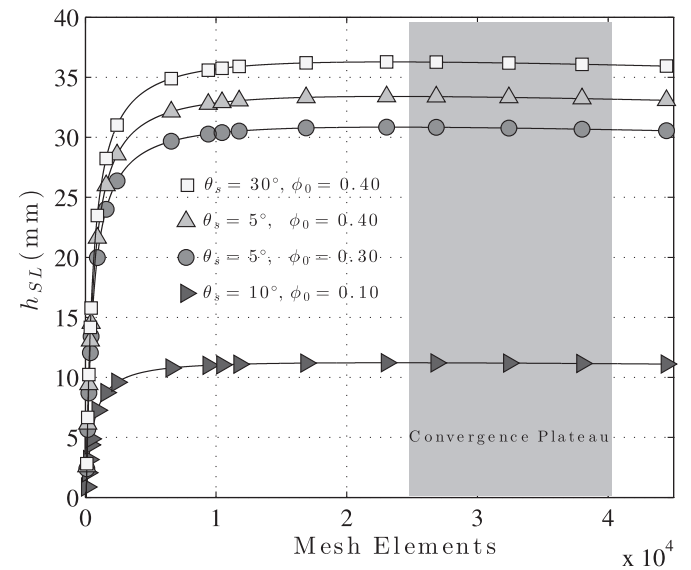


**Fig. 3.** Convergence of free triangular mesh.  $h_{SL}$  (mm) as function of number of mesh elements. The solid line represents the trend points for different physical conditions and grey region represents the area of convergence of the numerical solutions.

approaches to  $h_{SL} \approx 35.21$  mm,  $h_{SL} \approx 33.08$  mm,  $h_{SL} \approx 30.14$  mm and  $h_{SL} \approx 10.04$  mm for Case 1, Case 2, Case 3 and Case 4, respectively. Here, the convergence plateau starts using about 20,000 mesh elements. Inside this region it was not possible to observe a significant difference in the variable  $h_{SL}$  with increasing the value of mesh elements. Given that, the finest mesh implies an 8 h calculation in excess of the intermediate mesh within the plateau, and 12 h relative to the coarsest using a 4th generation Intel Core i7 Processor.

In this work we have used a compromise number of free triangular mesh composed by 30,000 elements in order to optimize the calculation time of all numerical simulations. The same procedure was performed to analyse the convergence of the solutions for geometry G1, thus obtaining the similar results. We have done the convergence analysis in MP<sub>3</sub> of the geometry G2 because of its relevance in the flux of particles in the sedimentation process. A physical validation of the results is given in the next section.

### 3. Results and discussion

A set of sedimentation numerical experiments was carried out under different physical conditions, including duct angles and particle concentrations. An experimental validation of this numerical model has recently been performed by Palma et al. [23]. They have studied the sedimentation of monodisperse particles in tilted containers, finding an excellent agreement between the experimental and numerical results for sediment thickness.

In order to measure and characterize the sediment layer in this type of geometry, a decision must be made to define the boundary between the sediment layer and the fluid clear layer. The height of the sediment layer,  $h_{SL}$ , has been defined when the particle concentration along MP<sub>3</sub> is greater than or equal to 0.40. This value of the volume fraction corresponds to the abrupt transition in the particle concentration from 0.40 to very small values near to zero.

Fig. 4 shows the sedimentation process of an initial homogeneous mixture of  $\phi_0 = 0.30$  for geometry G1 (Left panel) and G2 (Right panel). Both panels correspond to the particle concentration field for  $t = 200$  s,  $t = 400$  s,  $t = 600$  s and  $t = 800$  s, whereas  $t = 800$  s is the final time of the sedimentation process. In each figure, the insets show the detail of the particle concentration at the bottom of the duct as well as at the slope change zone, respectively, where the colour bar represents the concentration of particles. Here, the minimum and maximum concentration are 0 and 0.60, respectively. The numerical conditions are  $\theta_s = 30^\circ$ ,  $\phi_0 = 0.30$  and  $\eta_f = 100$  mPa · s. Such conditions have been chosen because they represent an experimental condition for a large angle, additionally a high concentration of particles, without necessarily being the largest concentration calculated. From this figure, we can infer that there is a difference of 25% in the height of the sediment layer at the extreme left of geometry G1 and G2 for  $t = 800$  s. This difference in the build-up of granular material is due to the shape in the geometries; while a duct with a horizontal section shows a 73% of the accumulation of particles, the

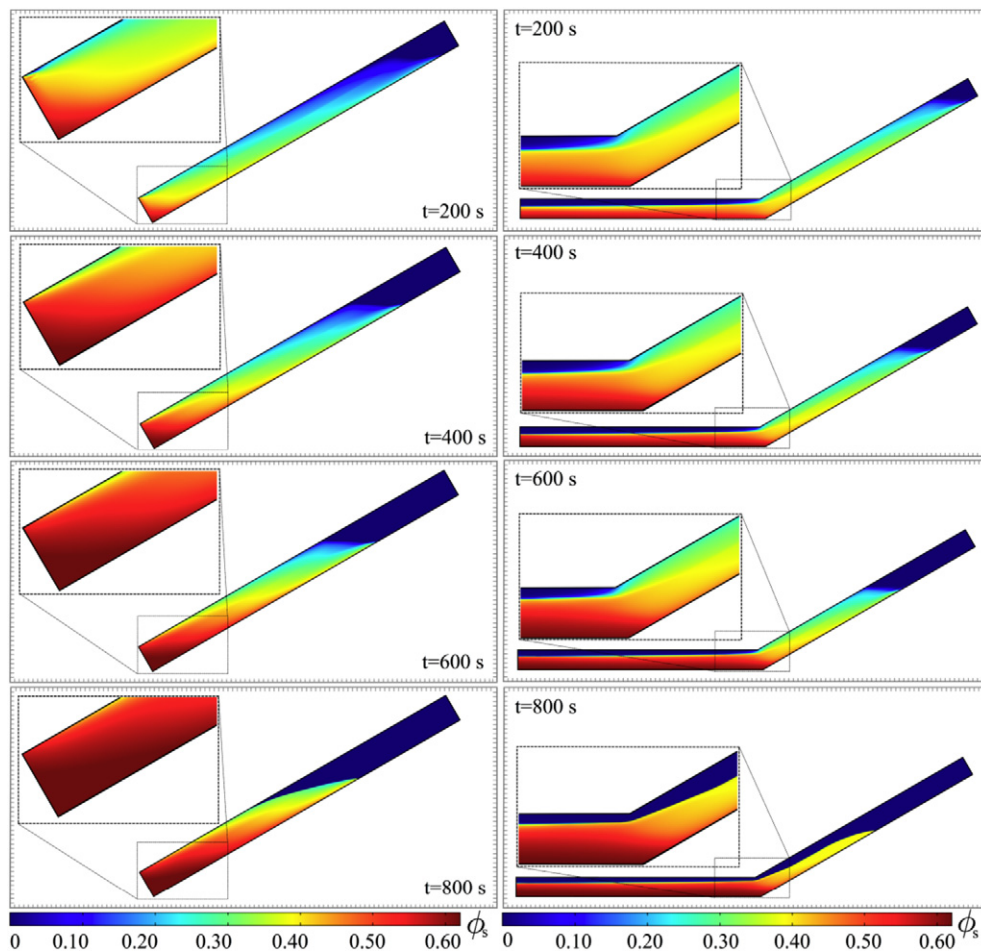


Fig. 4. Sedimentation process and particle concentration field for  $t = 200$  s,  $t = 400$  s,  $t = 600$  s and  $t = 800$  s. Left panel: geometry G1 and right panel: geometry G2. Inset: detail of  $\phi_s$ , at the bottom of the duct and at the slope change zone, respectively. The numerical conditions are  $\theta_s = 30^\circ$ ,  $\phi_0 = 0.30$  and  $\eta_f = 100$  mPa · s. The colour bar represents the concentration of particles.

tilted geometry shows an accumulation near to the 100% of its total capacity, 98%.

On the other hand, Fig. 5 shows the magnitude and direction of the velocity field of the dispersed phase (particles) for  $t = 50$  s,  $t = 100$  s,  $t = 150$  s and  $t = 200$  s for geometry G1 (Left panel) and G2 (Right panel), where the black arrows represent the particle flow direction and the colour bar represents the magnitude of the velocity of particles. Here, the minimum and maximum speed are 0 and 3.5 mm/s, respectively. We have shown the sedimentation process only for short times because at this time it is possible to observe more clearly the different stages of particle flow, both upward and downward the duct. The different stages of particle flow, both upward and downward the duct, have been described for other researchers considering only a tilted duct without a horizontal section (geometry G1) [10–12]. A comparison of the particle flow between G1 and G2 shows that although in the latter there is a horizontal section where the boundary condition is further away, the most important zone where the flow of particles is developed is in the inclined section. In particular, the inset of Fig. 5 shows that there is a fraction of particles that move towards the horizontal section. Such amount of particles is quantified below.

Fig. 6 (a), shows the maximum magnitude of the velocity of the dispersed phase for:  $\theta_s = 5^\circ$ ,  $\theta_s = 10^\circ$ ,  $\theta_s = 20^\circ$  and  $\theta_s = 30^\circ$  for geometry G1 and G2 as a function of time. Such maxima occurs at  $t = 100$  s,  $t = 130$  s,  $t = 160$  s and  $t = 200$  s for  $\theta_s = 30^\circ$ ,

$\theta_s = 20^\circ$ ,  $\theta_s = 10^\circ$  and  $\theta_s = 5^\circ$ , respectively. The measurements correspond to the line MP<sub>1</sub> (see Fig. 2) and the numerical conditions are  $\phi_0 = 0.30$  and  $\eta_f = 100$  mPa · s. In addition, from Fig. 6 (a) it is observed that the upward flow is always faster than the downward flow independently of the angle of the system. In general, the magnitude difference between the upstream and downstream is 31%, 24%, 17% and 13% for  $\theta_s = 5^\circ$ ,  $\theta_s = 10^\circ$ ,  $\theta_s = 20^\circ$  and  $\theta_s = 30^\circ$ , respectively, for both geometry G1 and G2. Once the process of settling on an inclined duct begins, a thin layer of free fluid particle appears in the upper wall of the duct. In this small layer free of particles, the fluid velocity is greater because it has a smaller section area than the suspension region, as can be seen in Fig. 1, (see also [13,36,37]). Fig. 6 (a) shows that the larger the angle of the duct, the velocities of the particles are larger both upward and downward. On the other hand, Fig. 6 (b) shows the measurements along MP<sub>2</sub>. Here, the behaviour is totally different as mentioned above. It cannot clearly see when the peak in the velocity of the dispersed phase occurs, as in the previous case. However, the downward flow is faster than the upward flow. It can be seen from this figure that the maximum velocities of the particles decrease with the angle of the system. In this case, the maximum speeds only reach 2 mm/s. This value is approximately 1.5 times smaller than the value obtained in MP<sub>1</sub> for an angle of  $30^\circ$ . Here, the particle flow during the early stages of motion is greater going downwards than upwards. This can be attributed to the proximity to the change in slope area where conditions of

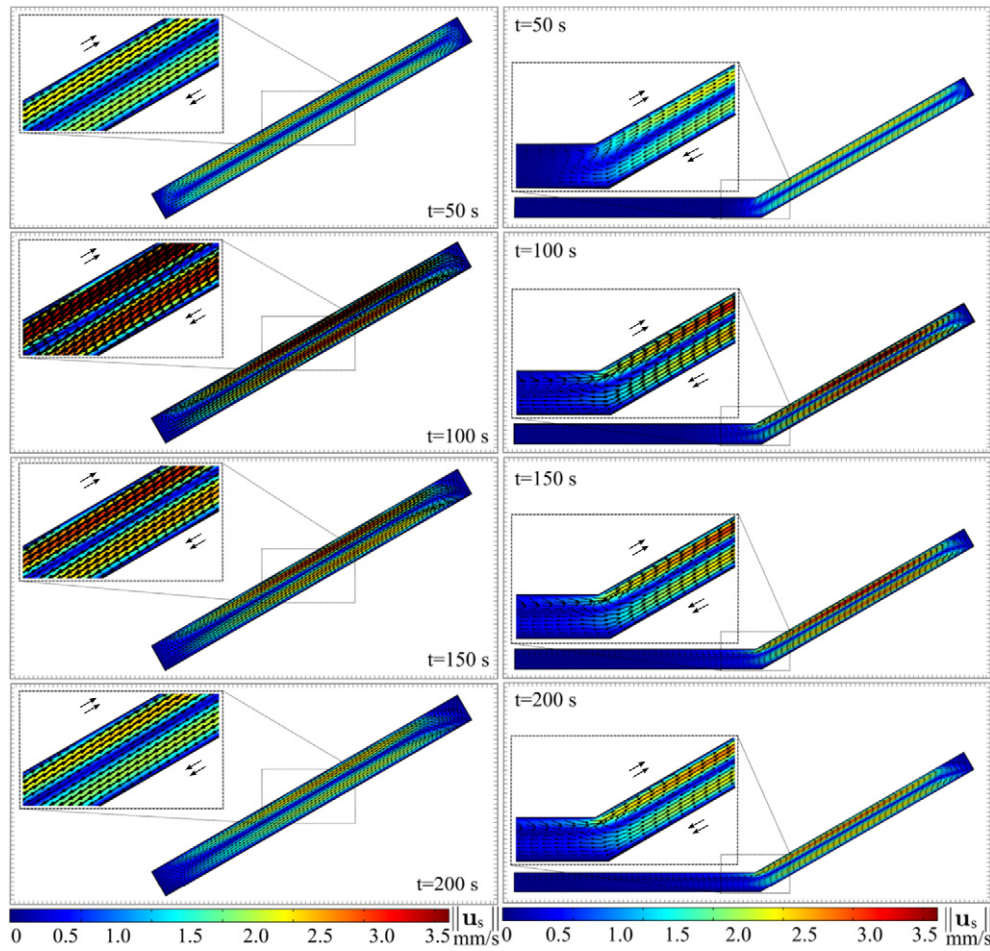
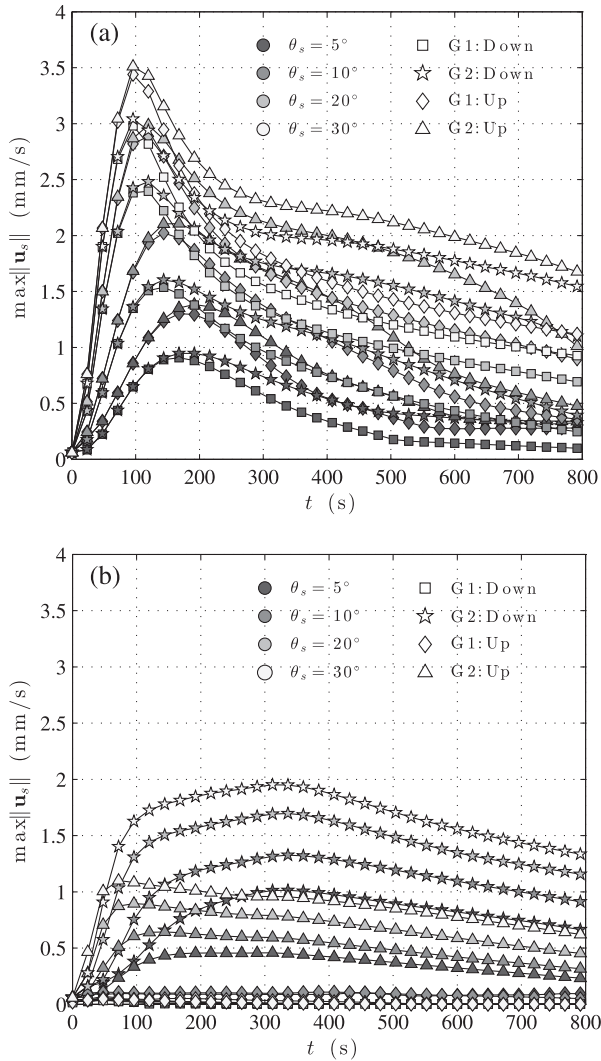


Fig. 5. Magnitude of the velocity field of the dispersed phase for  $t = 50$  s,  $t = 100$  s,  $t = 150$  s and  $t = 200$  s. Left panel: geometry G1 and right panel: geometry G2. Inset: detail of  $\mathbf{u}_s$ , at the middle of the duct and at the slope change zone, respectively. The black arrows represent the particle flow direction. The numerical conditions are  $\theta_s = 30^\circ$ ,  $\phi_0 = 0.30$  and  $\eta_f = 100$  mPa · s. The colour bar represents the magnitude of velocity of particles.



**Fig. 6.** Maximum magnitude of the velocity of the dispersed phase for:  $\theta_s = 5^\circ$ ,  $\theta_s = 10^\circ$ ,  $\theta_s = 20^\circ$  and  $\theta_s = 30^\circ$  for G1 and G2 as a function of time. The measurements correspond at (a): MP<sub>1</sub> and (b): MP<sub>2</sub>. The numerical conditions are  $\phi_0 = 0.30$  and  $\eta_f = 100 \text{ mPa}\cdot\text{s}$ .

symmetry in geometry are lost, unlike what happens in the previous case.

On the other hand, Fig. 7 shows the maximum magnitude of the velocity of the dispersed phase for:  $\theta_s = 5^\circ$ ,  $\theta_s = 10^\circ$ ,  $\theta_s = 20^\circ$  and  $\theta_s = 30^\circ$  for G2 as a function of time. The measurements correspond to MP<sub>3</sub> and MP<sub>4</sub>. Here, the measurements obtained from MP<sub>4</sub> show that the speeds are very small compared with those obtained from MP<sub>3</sub>. This behaviour of the particles is expected due to the largest flows related to the Boycott effect and are in fact in the inclined section. Here, the particle flow during the early stages of motion is 1.2 times higher for particles that are going upward than for particles going down. Regarding the accumulation of particles in the slope change, the top panel of Fig. 8 shows the accumulated particle mass  $\int \phi dz$  for (a)  $\theta_s = 10^\circ$  and (b)  $\theta_s = 30^\circ$  as a function of the horizontal distance of geometry G2. In all cases, we have made the calculations using an initial concentration of  $\phi_0 = 0.30$ . Additionally, we have shown only the time curves corresponding to  $t = 0 \text{ s}$ ,  $t = 200 \text{ s}$ ,  $t = 400 \text{ s}$ ,  $t = 600 \text{ s}$  and  $t = 800 \text{ s}$  for clarity. These figures show that the larger the angle of the system, the greater the build-up of granular material near to the slope change zone ( $x = 0$ ). Furthermore,

the amount of material transported along the horizontal section can be seen in the lower panel of Fig. 8. Here, we can infer that the area in the horizontal section affected by the flow of particles has a range of about 150 mm from the slope change ( $x = 0$ ) having a greater influence due to an angle (b)  $\theta_s = 30^\circ$  than to (a)  $\theta_s = 10^\circ$ . The accumulation of granular material in the slope change zone is better identified in Fig. 9 at final settling times.

Fig. 9 shows the height of the sediment layer along MP<sub>3</sub> normalized by the width of the duct,  $h_{SL}/L_0$ , as a function of: (a) the angle duct for different initial concentrations of particles and fluid viscosities, and (b) the initial concentrations of particles for distinct inclination angles of the system and fluid viscosities. In other words, the data represents the build-up of granular material in the slope change between the inclined section and the horizontal section of the duct, under different physical situations. Moreover, from Fig. 9 it is observed that the dependence between the normalized height and the initial concentration of particles is much more relevant than the dependence on the inclination of the system but that, in light of the resulting numbers, it is the combination of duct slopes and concentrations which control the risk of plug formation. In particular, we can see that for initial particle concentrations greater than 30% (0.30), an accumulation of solid material of 70% (0.70) is obtained at MP<sub>3</sub>. On the other hand, when the concentration is around 40%, the accumulation of solid material reaches a value of 80% and 94% of the duct width for  $\theta_s = 5^\circ$  and for  $\theta_s = 30^\circ$ , respectively, for a viscosity of  $\eta_{f1} = 100 \text{ mPa}\cdot\text{s}$  and, 74% and 88% of the duct width for  $\theta_s = 5^\circ$  and for  $\theta_s = 30^\circ$ , respectively, for a viscosity of  $\eta_{f3} = 300 \text{ mPa}\cdot\text{s}$ .

The present analysis thus suggests the existence of better and worse combinations of angles and concentrations, for the duct obstruction in the slope change zone. In light of the above results, we can find the obstruction condition of the duct, making a simple linear extrapolation (i.e.,  $h_{SL}/L_0 = 1$ ), from the data of Fig. 9b. Hence, the particle concentration values for which the duct is obstructed are  $\phi_0 = 47.9\%$  and  $\phi_0 = 45.0\%$  for  $\theta_s = 5^\circ$  and  $\theta_s = 30^\circ$ , respectively, for a viscosity of  $\eta_{f1} = 100 \text{ mPa}\cdot\text{s}$ . In Table 3, the results of duct obstruction for the rest of the variables are summarized. The results show that the conditions of obstruction (initial concentration of particles) increased 2.2% to increase the viscosity of 100 mPa·s to 200 mPa·s and 1.6% by increasing the viscosity of 200 mPa·s to 300 mPa·s, in all cases, regardless of the angle of inclination; being a total increase of 3.8%.

Finally, we will make an analysis of scale that allows to define an expression for the height of the sediment layer on the slope change based on certain dimensionless numbers. Thus, it has been shown with experiments and numerical simulations that the shear stress in mixtures and granular flows can be written as  $\tau = P\mu(I)$ , where the friction coefficient depends on a single dimensionless parameter,  $I$ , [38,39]. Although there is no friction term in our numerical model, we mentioned the work of Forterre & Pouliquen [38], Cassar et al. [39] to put in context the inertial number. The latter dimensionless parameter is called the inertial number and is defined as,

$$I = \frac{2a\dot{\gamma}}{\sqrt{P/\rho_s}} \quad (14)$$

where this dimensionless number can be interpreted as the ratio between two time scales: (a) a microscopic time scale  $t_{micro} = 2a/\sqrt{P/\rho_s}$  which represents the time it takes for a single particle to fall to a hole of size  $2a$  under the pressure  $P$  and which gives the typical time of rearrangements, and (b) a macroscopic time scale  $t_{macro} = 1/\dot{\gamma}$  related to the mean deformation. Here,  $\dot{\gamma}$  is the shear stress rate and  $a$  is the particle radius. It is observed that a relevant velocity scale in the problem is the sedimentation velocity,  $w_s = w_0 F$ , where  $w_0 = (2/9)a^2(\rho_s - \rho_f)g/\eta_f$ , it is the velocity for an

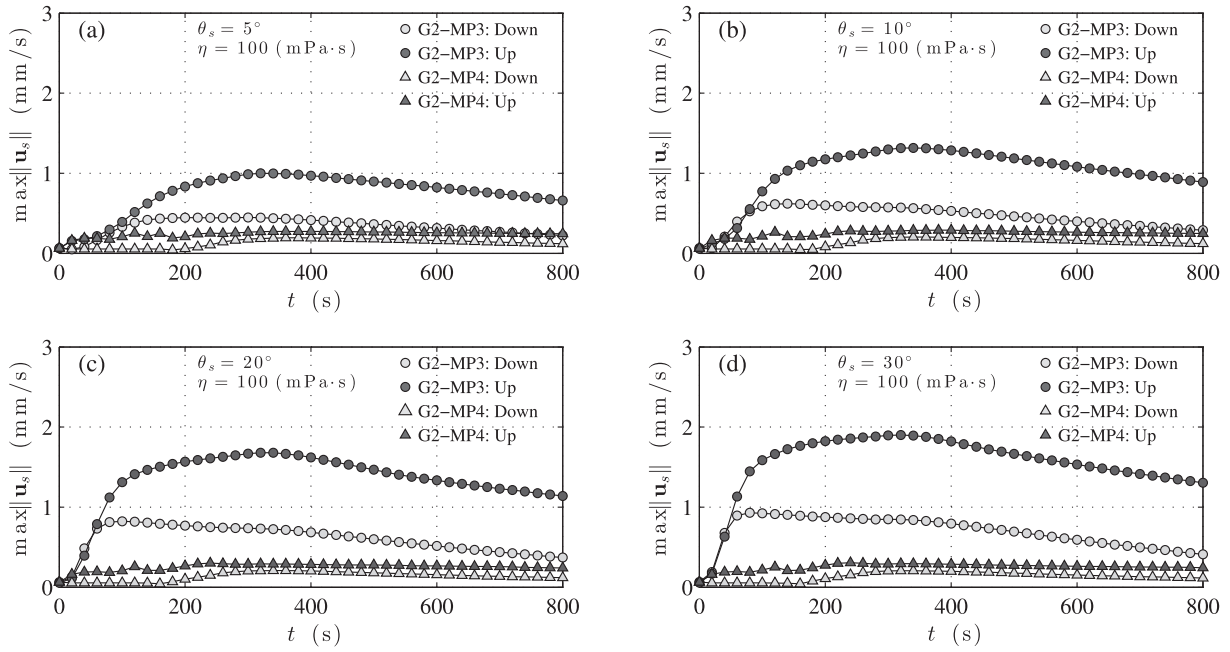


**Fig. 7.** Maximum magnitude of the velocity of the dispersed phase for (a):  $\theta_s = 5^\circ$ , (b):  $\theta_s = 10^\circ$ , (c):  $\theta_s = 20^\circ$  and  $\theta_s = 30^\circ$  for G2 as a function of time. The measurements correspond at MP3 and MP4. The numerical conditions are  $\phi_0 = 0.30$  and  $\eta_f = 100 \text{ mPa}\cdot\text{s}$ .

individual particle in an infinite medium and  $F$  is a hindrance function. In this work we have used the model proposed by Richardson & Zaki [40],  $F = (1 - \phi)^n$ , with a typical value of  $n = 5$ , [5].

In a recent work to describe sediment bed formation in inclined containers, Palma et al. [23] have expressed the inertial number as  $I \equiv Re_p(I_0 r)^{1/2} \sin\theta_s$ , where  $Re_p = 2a\rho_f w_s/\eta_f$  is the definition for the particle Reynolds number,  $r = \rho_s/\rho_f$  and  $I_0 = (3/4)\eta_f^2/\rho_f g (\rho_s - \rho_f) a^3$  and, the concentration particle number as  $\Phi = (\phi/\phi_m)^{1/3}$ . In this context, it has been found that such time scale balance is appropriate to describe a dimensionless version of the

sediment layer. On the other hand, it has been shown that the kinematics of a sedimentation process of monodisperse particles in an inclined duct (without a horizontal section) is described very well by two dimensionless numbers,  $R$  and  $\Lambda$ , [10,12,13,36,41]. Thus, the ratio of a sedimentation Grashof number to the Reynolds number can be written as  $\Lambda = 18 \left(\frac{H}{2a}\right)^2 \frac{\phi}{F}$ , Herbolzheimer & Acrivos [36]. Here, it is possible define  $H = L_1 \sin\theta_s$ , (see Fig. 2) and  $\Gamma = \frac{9\phi}{2F}$ .

Finally, the latter dimensionless number can be written as  $\Lambda \equiv \Gamma \left(\frac{L_1 \sin\theta_s}{a}\right)^2$ . In the present set of numerical experiments the latter

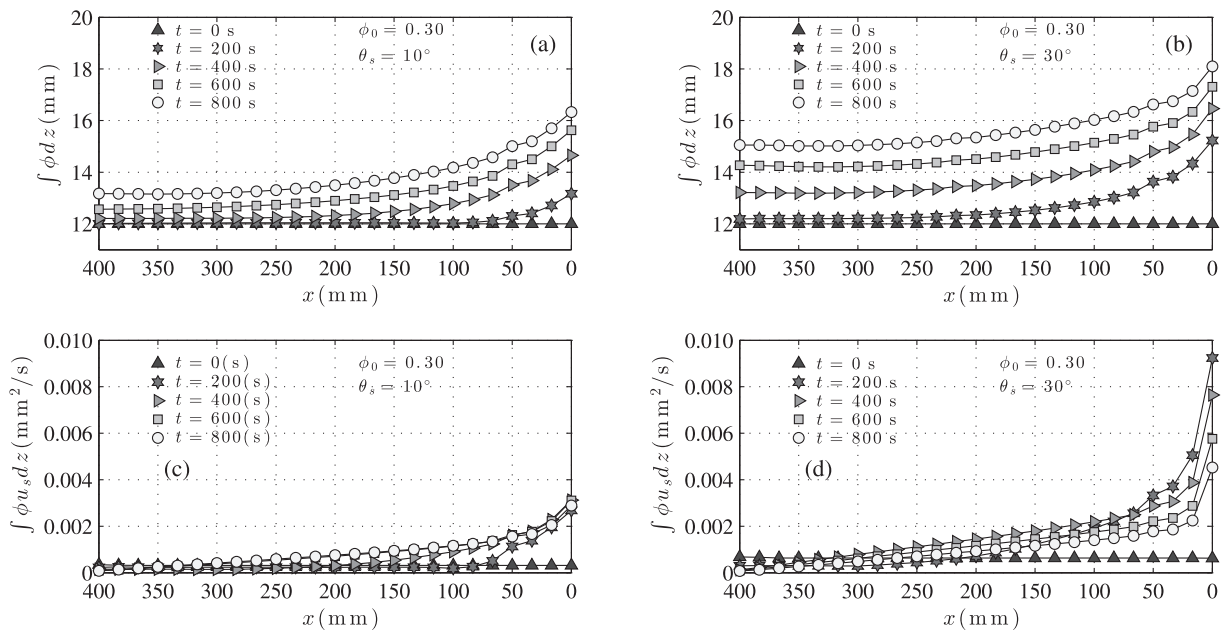


**Fig. 8.** Top panels: Accumulated particle mass  $\int \phi dz$  for (a):  $\theta_s = 10^\circ$  and (b):  $\theta_s = 30^\circ$ . Bottom panels: Mass flux  $\int \phi u_s dz$  along the horizontal section for (c):  $\theta_s = 10^\circ$  and (d):  $\theta_s = 30^\circ$ .

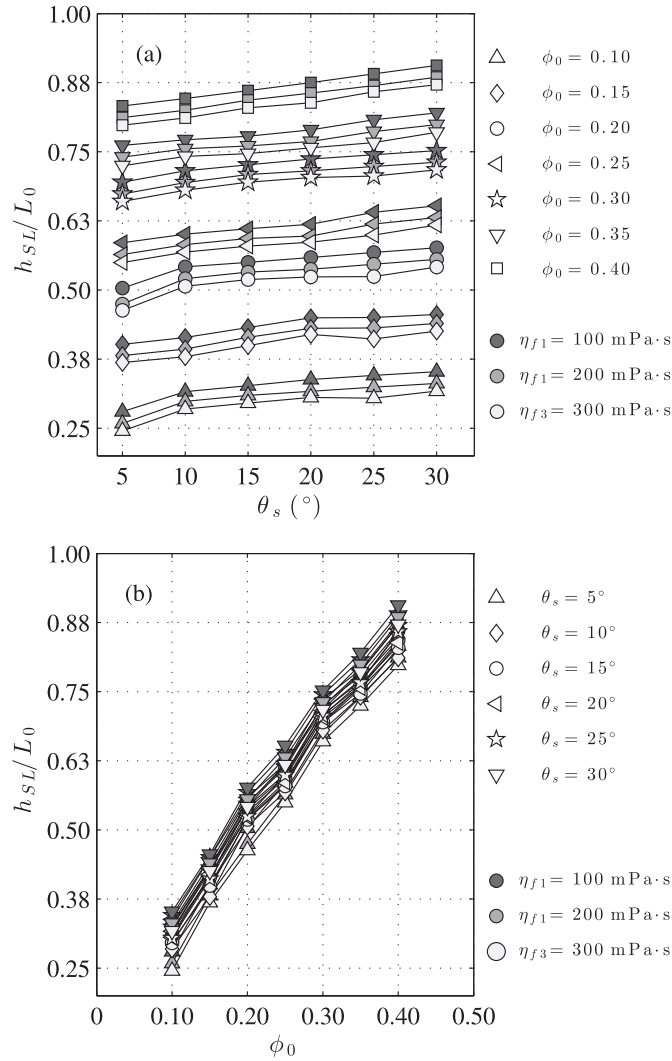


**Fig. 9.** Normalized height of the sediment layer as a function of (a): the angle of the system for different initial volume fraction of particles and fluid viscosities, and (b): the initial volume fraction of particles for different angles and fluid viscosities. The measurements correspond at MP<sub>3</sub>.

dimensionless numbers  $R$  and  $\Lambda$ , are in the range  $10^{-3} - 10^{-1}$  and  $10^4 - 10^6$ , respectively. In this manner, when the condition  $\Lambda \gg 1$  and  $RA^{-1/3} \ll 1$  are satisfied, the flow is laminar and viscous, and the sedimentation process in the inclined duct can be explained by the PNK theory. For our numerical experiments  $\Lambda \sim 10^6$  and  $RA^{-1/3} \sim 10^{-4}$ . Due to the evidence presented above, it is natural to propose  $\Lambda$  as a relevant dimensionless number for the inclined duct with a horizontal section. Although numerically we are in the same ranges where it has developed several quantitative approaches using asymptotic

**Table 3**  
Duct obstruction conditions.

|                       | $\eta_{f1} = 100 \text{ mPa}\cdot\text{s}$ | $\eta_{f2} = 200 \text{ mPa}\cdot\text{s}$ | $\eta_{f3} = 300 \text{ mPa}\cdot\text{s}$ |
|-----------------------|--|--|--|
|                       | $\phi_0$                                   | $\phi_0$                                   | $\phi_0$                                   |
| $\theta_s = 5^\circ$  | 47.9%                                      | 49.0%                                      | 49.8%                                      |
| $\theta_s = 10^\circ$ | 47.5%                                      | 48.6%                                      | 49.4%                                      |
| $\theta_s = 15^\circ$ | 46.9%                                      | 47.9%                                      | 48.8%                                      |
| $\theta_s = 20^\circ$ | 46.3%                                      | 47.5%                                      | 48.4%                                      |
| $\theta_s = 25^\circ$ | 45.2%                                      | 46.4%                                      | 47.1%                                      |
| $\theta_s = 30^\circ$ | 45.0%                                      | 45.6%                                      | 46.3%                                      |

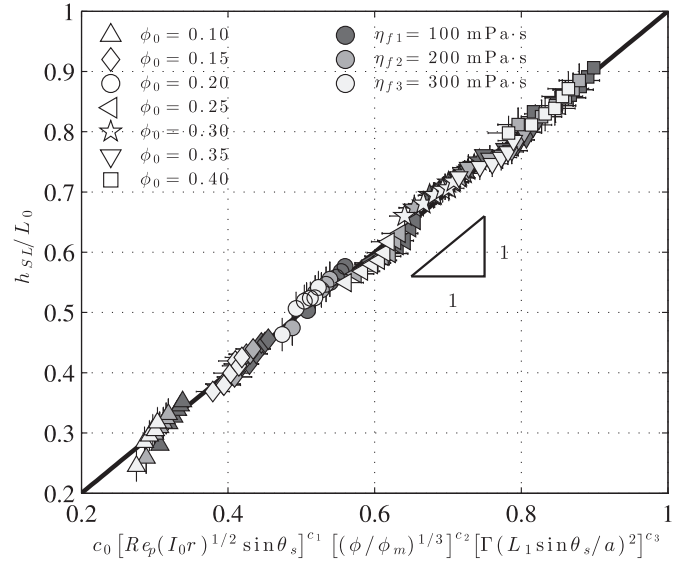


**Fig. 10.** Data fit for  $h_{SL}/L_0$  as a function of the dimensionless group  $\Pi = c_0 [Re_p(I_0 r)^{1/2} \sin \theta_s]^{c_1} [(\phi/\phi_m)^{1/3}]^{c_2} [\Gamma(L_1 \sin \theta_s/a)^2]^{c_3}$ . The solid line indicates the identity. The fitted coefficients are  $c_0 = 1.79 \pm 0.04$ ,  $c_1 = 1.02 \pm 0.03$ ,  $c_2 = 1.07 \pm 0.01$  and  $c_3 = 0.51 \pm 0.02$ .

analysis [10,12,36], the complicated geometry presented here precludes the development of a rigorous theoretical formulation to calculate the concentration of particles in the slope change zone and speed of the particles. In summary, the relevant dimensionless parameters are

$$I = Re_p(I_0 r)^{1/2} \sin \theta_s, \quad (15)$$

$$\Phi = \left(\frac{\phi}{\phi_m}\right)^{1/3}, \quad (16)$$

$$\Lambda = \Gamma\left(\frac{L_1 \sin \theta_s}{a}\right)^2. \quad (17)$$

The present results suggest that the numerical measurements of the height of the sediment layer at MP<sub>3</sub>,  $h_{SL}$ , can be represented by  $I$ ,  $\Phi$  and  $\Lambda$  dimensionless groups. In this work, we have left fixed the ratio  $L_0/L_1$  constant. Fig. 10 shows the best fit in terms of the dimensionless height of the sediment layer,  $h_{SL}/L_0$ , and the dimensionless group  $c_0 [Re_p(I_0 r)^{1/2} \sin \theta_s]^{c_1} [(\phi/\phi_m)^{1/3}]^{c_2} [\Gamma(L_1 \sin \theta_s/a)^2]^{c_3}$ . The corresponding fit was obtained using a multi-dimensional Levenberg-Marquardt nonlinear regression algorithm, [42,43]. The results indicate an excellent fit, with  $c_0 = 1.79 \pm 0.04$ ,  $c_1 = 1.02 \pm 0.03$ ,  $c_2 = 1.07 \pm 0.01$  and  $c_3 = 0.51 \pm 0.02$ , with an error of 0.1% compared to the theoretical slope of value 1. We can express the height of the sediment layer at MP<sub>3</sub> approximately as

$$h_{SL} = 1.8 L_0 I \Phi \sqrt{\Lambda}. \quad (18)$$

Finally, applying the obstruction condition of the duct (i.e.,  $h_{SL}/L_0 = 1$ ) to the Eq. (18), we obtain

$$\Phi = \frac{\alpha}{I\sqrt{\Lambda}}, \quad (19)$$

being  $\alpha \equiv 1/1.8$ . In this manner, using Eq. (19) is feasible to generalize the results of Table 3.

#### 4. Conclusions

In this paper we have solved numerically the continuity and momentum equations associated with the problem of sedimentation of fluid-solid mixtures at high concentrations in tilted ducts, under different physical conditions using COMSOL Multiphysics with the CFD package. The variables studied were the initial particle concentration, the fluid viscosity and the angle of the duct. A rich phenomenology associated with the dynamics of mixtures at high particle concentrations and at different angles was observed. The present results shown that the initial particle concentration is a very relevant variable for knowing under what conditions the duct could get obstructed and, in combination with some system angles, such conditions might represent a risk of duct plug. In particular, we have found that viscosity is not as important as the initial concentration of particles and the angle of the system.

Additionally, we found a mathematical expression using scaling arguments, formed by three dimensionless groups including the inertial number, particle concentration and the ratio between the sedimentation Grashof number to the Reynolds number to explain the height of the sediment layer in the slope change zone of a duct. Imposing a condition of obstruction, we have found a combination of initial concentrations of particles and fluid viscosities that shall block the duct in the slope change zone. Finally, we have related and extended these results with a dimensionless expression describing the phenomenon of obstruction. Although the present results are expressive of the effect of solids concentration and duct angles, a more in depth analysis is required to unveil the physics of the particle organization near the zone where the slope change occurs. This is currently being done experimentally by the present group of researchers.

#### Acknowledgements

The authors acknowledge the support of the National Commission for Scientific and Technological Research of Chile, CONICYT, Grant No. 21110766, Fondecyt Grant Nos. 11110201, No. 1130910, No. 1160971 and No. 1161751, the Department of Civil Engineering, the Department of Mining Engineering and the Advanced Mining Technology Center of the University of Chile.

#### References

- [1] R.A. Kulwiec, *Materials Handling Handbook*, John Wiley & Sons. 1985.
- [2] B.E. Abulnaga, *Slurry Systems Handbook*, McGraw-Hill. 2002.
- [3] C.F. Ihle, Should maximum pressures in ore pipelines be computed out of system startups or power outages? *Miner. Eng.* 55 (2014) 57–59.
- [4] D.M. Admiraal, Influence of pipe angle on bedload transport in an inclined pipe, *Int. J. Sediment Res.* 18 (2003) 122–129.
- [5] E. Guazzelli, J. Hinch, Fluctuations and instability in sedimentation, *Annu. Rev. Fluid Mech.* 43 (2011) 97–116.
- [6] W.F. Leung, R.F. Probst, Lamella and tube settlers. 1. Model and operation, *Ind. Eng. Chem. Process. Des. Dev.* 22 (1) (1983) 58–67.
- [7] W.F. Leung, Lamella and tube settlers. 2. Flow stability, *Ind. Eng. Chem. Process. Des. Dev.* 22 (1) (1983) 68–73.
- [8] E. Ponder, On sedimentation and rouleaux formation, *Q. J. Exp. Physiol.* 15 (3) (1925) 235–252.
- [9] H. Nakamura, K. Kuroda, La cause de l'accélération de la vitesse de sédimentation des suspensions dans les récipients inclinés, *Keijo J. Med.* 8 (1937) 256–296.
- [10] A. Acrivos, E. Herbolzheimer, Enhanced sedimentation in settling tanks with inclined walls, *J. Fluid Mech.* 92 (03) (1979) 435–457.
- [11] E. Guazzelli, J.F. Morris, *A Physical Introduction to Suspension Dynamics*, vol. 45. Cambridge University Press. 2011.
- [12] E. Herbolzheimer, Stability of the flow during sedimentation in inclined channels, *Phys. Fluids* (1958–1988) 26 (8) (1983) 2043–2054.
- [13] R.H. Davis, A. Acrivos, Sedimentation of noncolloidal particles at low Reynolds numbers, *Annu. Rev. Fluid Mech.* 17 (1) (1985) 91–118.
- [14] E.S.G. Shaqfeh, A. Acrivos, The effects of inertia on the buoyancy-driven convection flow in settling vessels having inclined walls, *Phys. Fluids* (1958–1988) 29 (12) (1986) 3935–3948.
- [15] A. Nir, A. Acrivos, Sedimentation and sediment flow on inclined surfaces, *J. Fluid Mech.* 212 (1990) 139–153.
- [16] B. Kapoor, A. Acrivos, Sedimentation and sediment flow in settling tanks with inclined walls, *J. Fluid Mech.* 290 (1995) 39–66.
- [17] K.R. Rajagopal, L. Tao, *Mechanics of Mixtures*, vol. 35. World Scientific. 1995.
- [18] H. Enwald, E. Peirano, A.-E. Almstedt, Eulerian two-phase flow theory applied to fluidization, *Int. J. Multiphase Flow* 22 (1996) 21–66.
- [19] S. Ergun, Fluid flow through packed columns, *Chem. Eng. Prog.* 48 (1952) 89–94.
- [20] R.J. Atkin, R. Craine, Continuum theories of mixtures: basic theory and historical development, *Q. J. Mech. Appl. Math.* 29 (2) (1976) 209–244.
- [21] R.M. Bowen, Theory of mixtures, *Continuum Phys.* 3 (Pt I). (1976)
- [22] A. Bedford, D.S. Drumheller, Theories of immiscible and structured mixtures, *Int. J. Eng. Sci.* 21 (8) (1983) 863–960.
- [23] S. Palma, C.F. Ihle, A. Tamburrino, S.B. Dalziel, Particle organization after viscous sedimentation in tilted containers, *Phys. Fluids* 28 (7) (2016) 073304.
- [24] I.M. Krieger, Rheology of monodisperse latices, *Adv. Colloid Interface Sci.* 3 (2) (1972) 111–136.
- [25] I.M. Krieger, T.J. Dougherty, A mechanism for non-Newtonian flow in suspensions of rigid spheres, *Trans. Soc. Rheol.* (1957–1977) 3 (1) (1959) 137–152.
- [26] N.A. Frankel, A. Acrivos, On the viscosity of a concentrated suspension of solid spheres, *Chem. Eng. Sci.* 22 (6) (1967) 847–853.
- [27] J.J. Stickel, R.L. Powell, Fluid mechanics and rheology of dense suspensions, *Annu. Rev. Fluid Mech.* 37 (2005) 129–149.
- [28] D. Gidaspow, *Multiphase Flow and Fluidization: Continuum and Kinetic Theory Descriptions*, Academic Press. 1994.
- [29] C.Y. Wen, Y. Yu, *Mechanics of Fluidization*, vol. 62. 2013. Page 100 of: Chem. Eng. Prog. Symp. Ser..
- [30] B. Ettehadieh, D. Gidaspow, R. Lyczkowski, Hydrodynamics of fluidization in a semicircular bed with a jet, *AIChE J.* 30 (4) (1984) 529–536.
- [31] D. Gidaspow, B. Ettehadieh, Fluidization in two-dimensional beds with a jet. 2. Hydrodynamic modeling, *Ind. Eng. Chem. Fundam.* 22 (2) (1983) 193–201.
- [32] D. Gidaspow, Y.-T. Shih, J. Bouillard, D. Wasan, Hydrodynamics of a lamella electrosettler, *AIChE J.* 35 (5) (1989) 714–724.
- [33] M. Massoudi, K.R. Rajagopal, J.M. Ekmann, M. Mathur, Remarks on the modeling of fluidized systems, *AIChE J.* 38 (3) (1992) 471–472.
- [34] O.C. Zienkiewicz, R.L. Taylor, *The Finite Element Method: Solid Mechanics*, vol. 2. Butterworth-Heinemann. 2000.
- [35] C. Johnson, *Numerical Solution of Partial Differential Equations by the Finite Element Method*, Courier Corporation. 2012.
- [36] E. Herbolzheimer, A. Acrivos, Enhanced sedimentation in narrow tilted channels, *J. Fluid Mech.* 108 (1981) 485–499.
- [37] T. Peacock, F. Blanchette, J.W. Bush, The stratified boycott effect, *J. Fluid Mech.* 529 (2005) 33–49.
- [38] Y. Forterre, O. Pouliquen, Flows of dense granular media, *Annu. Rev. Fluid Mech.* 40 (2008) 1–24.
- [39] C. Cassar, M. Nicolas, O. Pouliquen, Submarine granular flows down inclined planes, *Phys. Fluids* (1994–present) 17 (10) (2005) 103301.
- [40] J.F. Richardson, W.N. Zaki, Sedimentation and fluidisation: part I, *Chem. Eng. Res. Des.* 75 (1997) S82–S100.
- [41] W.D. Hill, R.R. Rothfus, K. Li, Boundary-enhanced sedimentation due to settling convection, *Int. J. Multiphase Flow* 3 (6) (1977) 561–583.
- [42] Y. Bard, *Nonlinear Parameter Estimation*, vol. 1209. Academic Press New York. 1974.
- [43] J.J. More, *The Levenberg-Marquardt Algorithm: Implementation and Theory*, Springer. 1978. pages 105–116 of: Numerical analysis.